ROYAL SOCIETY OF CHEMISTRY

PAPER

Check for updates

Low-toxicity chemical solution deposition of ferroelectric Ca:HfO₂†

Miguel Badillo, [ab] Sepide Taleb, [a] Taraneh Mokabber, [a] Jan Rieck, [b] Rebeca Castanedo, [c] Gerardo Torres, [c] Beatriz Noheda *[b] and Mónica Acuautla *[a]

So far, a few chemical solution routes for the fabrication of ferroelectric HfO₂ films have been reported. Most of them employ precursors, solvents or additives that are considered difficult to handle, unstable, toxic, generally unfriendly with the environment and/or unsuitable for large scale industrial processes. In this work, we present a new effective chemical route for the preparation of ferroelectric doped-HfO₂ films. The solution is prepared from simple, stable, and available precursors, handled in an open atmosphere and requires no restrictive processing conditions. We used 5 at% Ca as the dopant of HfO₂ to induce a maximum remnant polarization of 9.3 and 11.1 μC cm^{-2} for 54 and 90 nm thick Ca:HfO₂ films, respectively. The current-electric field loops show intense and distinctive ferroelectric switching peaks and the corresponding ferroelectric loops show excellent saturation, which speaks of good device quality with low leakage. Crystallization and the wake-up of ferroelectricity in Ca:HfO₂ films were achieved by means of rapid thermal annealing at different temperatures and times in an Ar:O₂ atmosphere. In comparison to thin films, thicker ones exhibited the highest remnant polarization at shorter annealing times, thus evidencing the need for precise control of thermal processing. The Ca:HfO₂ films with a thickness of 50 nm displayed a good balance between leakage and retention, maintaining the ferroelectric response above 10^5 cycles at 1 kHz. The developed precursor solution is promising for its use in spray-coating and ink-jet printing techniques.

1 Introduction

Since its first report as a new lead-free ferroelectric material in 2011 by Böske *et al.*,[1] doped-HfO₂ (doped-hafnia), as well as its oxide sister ZrO₂,[2] has been regarded as a very promising functional oxide in a myriad of applications, including FeRAM,[3] MEMs,[4] NEMs,[5] energy harvesting,[6] *etc.*[7] Under standard conditions, HfO₂ crystallizes into a stable monoclinic phase (m-). It goes through tetragonal (t-) and cubic phase (c-) structure transformations, which entails a large volume change, for increasing temperatures.[8] While the t- and c-phases share the VIII coordination of the parent fluorite structure, the m-phase is strongly distorted with coordination VII. The reported polar orthorhombic (o-) and rhombohedral (r-) phases are metastable phases that provide bridging structures between the m- and the t-phase with intermediate volume.[1,9,10] In order to achieve polar phases, the strategy is to provide stabilization of the tetragonal or cubic phases and then gradually increase the volume to reach the intermediate phases, this while avoiding the significantly more stable m-phase.[11,12] It has been demonstrated that this can be achieved by different mechanisms.[13]

One of the mechanisms for the stabilization of the polar phase of hafnia is chemical modification. Several doping elements have been used to stabilize hafnia's ferroelectric orthorhombic and rhombohedral phases. However, it has been experimentally and theoretically demonstrated that bigger ionic-radii elements best stabilize the polar phases in HfO₂.[12,14,15] Moreover, HfO₂ can be mixed in all ratios with ZrO₂. It has been found that Hf₀.₅Zr₀.₅O₂ (HZO) can also attain good ferroelectricity.[9,16,17] In 2017, using first-principles computations, Batra *et al.* concluded that Ca, Sr, Ba, Y, and elements from the lanthanide series (La and Gd), should produce the highest remnant polarization (P_r) values for ferroelectric HfO₂.[18] Similar theoretical conclusions were reached by other groups.[12,19] Nevertheless, to the best of our knowledge, there is only one other experimental report on ferroelectric

[a] Engineering and Technology Institute Groningen (ENTEG), Faculty of Science and Engineering, University of Groningen, Nijenborgh 4, Groningen 9747AG, The Netherlands. E-mail: m.i.acuautla.meneses@rug.nl

[b] Zernike Institute for Advanced Materials (ZIAM), Faculty of Science and Engineering, University of Groningen, Nijenborgh 4, Groningen 9747AG, The Netherlands. E-mail: b.noheda@rug.nl

[c] Centro de Investigación y de Estudios Avanzados del I.P.N., Unidad Querétaro, 76230, Querétaro, Mexico

† Electronic supplementary information (ESI) available. See DOI: https://doi.org/10.1039/d2tc04182k

This journal is © The Royal Society of Chemistry 2023

J. Mater. Chem. C, 2023, **11**, 1119–1133 | 1119

Ca-doped-HfO$_2$ (Ca:HfO$_2$) by Yifan Yao et al.[20] Although the authors report a P_r value of 10.5 μC cm^{-2} for a 35 nm-thick film with 4.8 mol% Ca-doping, the effect of Ca-doping on the device leakage is unclear.

Ferroelectric HfO$_2$ films with high P_r values have been fabricated by pulsed laser deposition (PLD),[9] atomic layer deposition (ALD),[21] sputtering deposition,[22] and chemical solution deposition (CSD).[14] Even though ALD and PLD have achieved the highest P_r values, sputtering and CSD are better at producing thicker ferroelectric HfO$_2$ films, which holds promise for MEM devices.[4] There are a few chemical techniques available for the synthesis of HfO$_2$. Sol–gel involves the controlled hydrolysis, in an inert atmosphere, of air-sensitive metal precursors like HfCl$_4$ and Hf-alkoxides.[23,24] Compared to other techniques, the control of chemistry in the sol–gel method is exquisite, but counts with the disadvantage of more restrictive synthesis conditions. Moreover, precursors and solvents like HfCl$_4$ and 2-methoxy-ethanol can release corrosive and toxic by-products. In the method of inorganic decomposition, substances like ammonia, H$_2$O$_2$, and nitric acid are used to produce Hf(NO$_3$)$_4$ in water from inorganic metal precursors.[20] The metal nitrate is decomposed at moderate temperatures to deliver HfO$_2$ and nitrogen compounds. Unfortunately, in addition to poor control of chemistry, the reagents and by-products can be highly corrosive to the processing equipment, and the purity of Hf(NO$_3$)$_4$ is hard to control. Another method is metallo-organic decomposition (MOD), where hafnium metallo-organic precursors, commonly hafnium 2,4-pentanedionate (also known as hafnium acetylacetonate or Hf(acac)$_4$) are employed as the metal source.[15] Because of full metal saturation of the coordination sphere of hafnium with acetylacetone ligands, Hf(acac)$_4$ is an air-stable, non-hygroscopic, metal β-diketonate.[25–27] In the MOD method, the corresponding metal precursor is dissolved by compatible solvents. The homogeneous mixtures are later heated at high temperature to decompose into HfO$_2$ and various organic by-products that depend on the selection of the initial raw materials. Although MOD processes require higher decomposition temperatures, the toxicity and harmfulness of the precursor solution can be controlled by appropriate raw material selection.

In the literature concerning the fabrication of ferroelectric HfO$_2$ films by MOD, the corresponding metal acetylacetonates are dissolved at moderate temperatures (100–160 °C) in either propionic acid[4] or, most frequently, mixtures of propionic acid and propionic anhydride.[15] Although propionic acid can be considered safe for humans in small quantities, it can be hazardous in the concentrated form. Besides, due to its volatility, propionic acid produces flammable, unpleasant, irritating fumes (CAS: 79-09-4). On the other hand, just as acetic anhydride is, propionic anhydride (CAS: 123-62-6) is a toxic, corrosive, flammable, reactive, and unstable compound that requires special handling conditions (such as avoiding uncontrolled contact with water, alcohols, and amines).[28] Thus, the replacement of propionic anhydride with less dangerous precursors would represent a significant improvement that must be addressed. Likewise, limiting the use of propionic acid would also be of great importance for industrial processes. Moreover, mixtures of propionic acid and propionic anhydride typically require heating for dissolution. Nonetheless, the metal precursors might undergo undesired side chemical reactions that could make the process difficult to reproduce.[29] Therefore, aiming for lower dissolution temperatures is also recommended. In this context, a simple procedure involving dissolution of Hf(acac)$_4$ in acetic acid under mild conditions was recently reported by Zheng et al.[30] However, despite a large P_r for Ce:HfO$_2$, the reported ferroelectric loops are not saturated, thus further optimization might be required.[30]

Lactic acid (CAS: 50-21-5) is a carboxylic acid structurally similar to propionic acid and acetic acid, but it contains an extra O atom in the form of a –OH group. Due to the presence of a carboxy group, it is expected that lactic acid can coordinate to Hf^{4+} and displace the acetylacetonate molecules. Also, as is the case for propionic acid, lactic acid is regarded as a safe material for humans, and its associated risks come primarily from its acidity in concentrated form. The human body metabolizes D and L lactic acid, which is thus considered biodegradable. Currently, pure lactic acid is produced mainly by the petrochemical industry, but great strides have been made for its synthesis and separation from biogenic sources. Structurally, the extra –OH group in lactic acid makes it a viscous liquid through hydrogen bonding.[31] Therefore, in contrast to propionic acid, lactic acid does not evaporate easily under environmental conditions (low flammability), and neither does it have a strong odor. Unfortunately, the viscous nature of pure lactic acid makes it inappropriate for chemical deposition processes, where rheological control is essential. Nevertheless, lactic acid is compatible, and sometimes even miscible, with other simple polar compounds like water and alcohols, which can be used to reduce its viscosity.[31] In the past, we have used mixtures of lactic acid and triethylamine in alcoholic solvents for the effective dissolution of transition metal (Cu and Cd) compounds and ionic salts (SnCl$_2$) at room or mild temperatures.[32,33] Therefore, the mixture of additives has been helpful for dissolution of different precursor metal compounds and the corresponding synthesis of metal oxides.

In this paper, we report the use of a greener precursor solution to fabricate ferroelectric doped-HfO$_2$. The new solution is based on Hf(acac)$_4$, isopropanol as the main solvent, and small amounts of lactic acid and triethylamine as stabilizing agents. Moreover, the dissolution happens at temperatures below 100 °C and does not require special synthesis conditions. The precursor solution complies better with the definition of green chemistry in the 2000s by the International Union of Pure and Applied Chemistry (IUPAC): "The invention, design, and application of chemical products and processes to reduce or to eliminate the use and generation of hazardous substances".[34,35] Using spin-coating and rapid thermal annealing (RTA), ferroelectric Ca:HfO$_2$ (5 mol%) metal–insulator–metal (MIM) capacitors were fabricated. We found a strong, saturated ferroelectric response with remnant polarization values of 9 and 11 μC cm^{-2} for Ca:HfO$_2$ films of 54 and 90 nm, respectively. Due to the flexibility for adjustment of the solution chemistry, our HfO$_2$ precursor solution is well suited for

1120 | J. Mater. Chem. C, 2023, **11**, 1119–1133

This journal is © The Royal Society of Chemistry 2023

large-scale deposition techniques, such as spray-coating and ink-jet printing.

2 Experimental

2.1 Synthesis and thermal behavior of precursor solution

All metal precursors, solvents, and additives were used without purification steps. All the procedures for the preparation of the precursor solution were performed under normal air conditions. Hafnium 2,4-pentanedionate (Alfa-Aesar, 97%) and calcium 2,4-pentanedionate (Sigma-Aldrich, 99.95%) were weighed, in corresponding proportions, to produce a 5 mol% Ca-doped HfO_2 precursor solution (concentration in the final Ca:HfO_2 films was estimated to be around 5.86% by X-ray photoelectron spectroscopy analysis). The calcium doping concentration was based on the work of Yao et al.[20] Ca(acac)$_2$ was first added to a round flask. Then, measured volumes of isopropanol (IPA, Macron, 99.9%), triethylamine (TEA, Merck, 99%) and lactic acid (LA, Fischer-Scientific, 90%) were added to the flask. Dissolution of Ca(acac)$_2$ took 30 minutes under stirring under room conditions. Hf(acac)$_4$ powder was later added to the mixture. The dissolution took place in a few minutes. The molar ratios of all substances with respect to Hf were 1/4.3/8.4/214 for Hf(acac)$_4$/TEA/LA/IPA, respectively. The estimated concentration of Hf in the solution was 0.056 mol L^{-1}. The mixture was heated between 95–100 °C for 4 hours using a silicon oil bath to ensure complete dissolution of the salts. To avoid loss of solvents, reflux conditions were established with ice-chilled water. The refluxed solution was allowed to cool down to room temperature, and then filtered 2 times with 0.2 µm pore size filters (Whatman). The solution was stored in a tight glass container with a polypropylene cap. If protected from light, the solution remains transparent and colorless for several months. The preparation of the solution is discussed in more detail in Section 3.1.

Thermal behavior of the solution was evaluated by thermogravimetric analysis and differential scanning calorimetry (DSC) using a DSC SDT 2960 TA Instrument. In alumina crucibles, samples of 15–20 mg were heated at 10 °C min^{-1} from room temperature to 800 °C under a dry-air flow of 100 ml min^{-1}. Sapphire was used as a reference.

2.2 Fabrication of Ca:HfO_2 films by chemical solution deposition and spin-coating

Ca:HfO_2 films were deposited by spin-coating on metalized silicon wafers. The structure of the substrate stack was Pt(100 nm)/Ti(5 nm)/SiO$_2$(95 nm)/Si(100 orientation). Pt and Ti were deposited using an electron-beam evaporation method. The quality of the substrate is crucial for the performance of the films, thus we have included a procedure for wafer metallization, cutting, cleaning, and storage in the ESI.† Ca:HfO_2 films were deposited at 4000 rpm for 30 s on 8 mm × 8 mm substrates. Each layer was dried immediately at 150 °C for 5 minutes, followed by pyrolysis at 300 °C for 5 minutes on a hot plate. Before deposition of a new layer, the previous layer was U.V./Ozone treated for 5 minutes (Ossila U.V./Ozone cleaner).

The process was repeated 1, 3 or 5 times to produce films of 18, 54 and 90 nm, respectively. The viscosity of lactic acid was responsible for the deposition of relatively thick films in few repetitions.

2.3 Crystallization of Ca:HfO_2 films by rapid thermal annealing

Multi-stack Ca:HfO_2 films were subject to Rapid Thermal Annealing (RTA) at 700 °C for 90 s, 800 °C for 60 s, or 800 °C for 90 s in an Ar:O$_2$ atmosphere (1:1) at 0.5 atm. The RTA system uses an arrangement of 12 Phillips 500 W halogen lamps enclosed in two stainless-steel semi-boxes, each one focusing infrared radiation from below and above the samples. Temperature is precisely controlled by carefully tuned Novus 1200 controllers.[36–38] The space for samples allows several samples to be heated at once. The annealing program for Ca:HfO_2 films consisted of preconditioning at 150 °C for 5 minutes, followed by a heating ramp of 9.2 °C s^{-1} or 10.8 °C s^{-1} to 700 °C and 800 °C, respectively. The arrangement of the films during RTA processing is described in Fig. 1. The samples were placed on top of a TiO$_2$-coated graphite plate. Above them, quartz windows are located, leaving free space above the surface of the films. The measuring thermocouple was placed close to the samples. Because of the different mechanisms of heating involved (radiation, conduction, and convection), the films received asymmetrical heating. The goal was to maximize the annealing of the Ca:HfO_2 films while limiting the heating of the platinized silicon substrate. The cooling down of the samples happens naturally through heat loss to the environment through the system boundaries. Exemplification of the heating program, as well as the cooling off of the samples is depicted in Fig S1 of the ESI.†
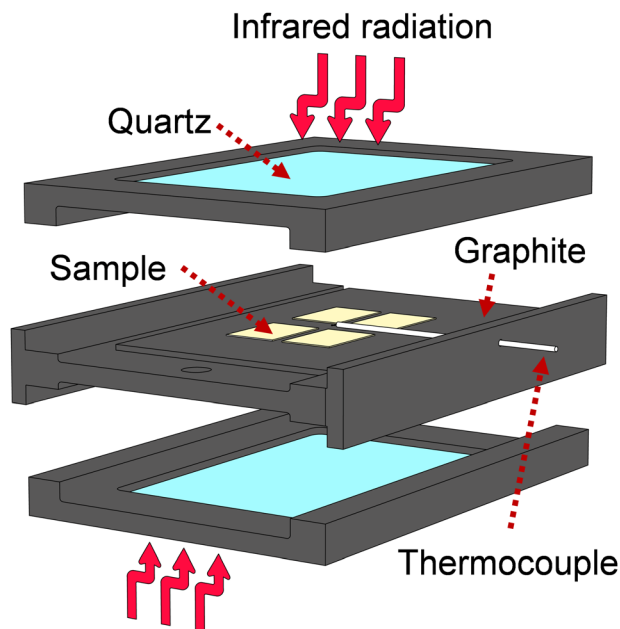

Fig. 1 Scheme of samples inside the heating device during rapid thermal annealing. Different heating mechanisms take place due to contact of the samples with graphite (conduction), irradiation with I.R. light (radiation) and exchange of heat with the surrounding gas (convection).

This journal is © The Royal Society of Chemistry 2023

J. Mater. Chem. C, 2023, 11, 1119–1133 | 1121

2.4 Characterization of films and MIM devices

X-ray diffraction measurements were performed in a Pananalytical X'Pert Pro MRD in grazing incidence geometry at an angle of $\theta = 0.55°$. The surface topography of the films was evaluated with a Bruker's Dimensions Icon Atomic Force Microscope (AFM). Symmetric, Pt/Ca:HfO$_2$/Pt, metal-insulator-metal (MIM) capacitors were fabricated by U.V. photolithography. Round, top Pt electrodes of 60 nm thickness and 50 μm radius were deposited by e-beam evaporation. Post-annealing of the MIM stack was performed on a hot plate at 100 °C for 5 minutes. A state-of-the-art aixACCT TF Analyzer 2000 was used for ferroelectric testing of the Ca:HfO$_2$ films in the MIM stacks. Ferroelectric wake-up of the capacitor structures was achieved by application of 10^3 bipolar, rectangular pulses of 2.78 MV cm^{-1} amplitude at 1 kHz (15 and 25 V for 54 and 94 nm thin films, respectively). Dynamic Hysteresis Measurements (DHM) were performed with bipolar triangular pulses of 2.4 MV cm^{-1} amplitude at 1 kHz with an average of 3 repetitions. After wake-up conditioning, fatigue measurements at 1, 10, 50, and 100 kHz were made with the same rectangular scheme of 2.78 MV cm^{-1} pulses. Piezo Force Microscopy (PFM) imaging was performed with an Asylum Research Cypher SPM machine on an 18 nm Ca:HfO$_2$ film with a bottom Pt electrode. A conductive Sb-doped Si tip with Co/Cr coating was used. An up-polarization square of 3.5×3.5 μm on an area of 5×5 μm was written. A DC bias of +10 V was first applied to the smaller area with a scanning

frequency of 0.5 Hz. Then the full PFM image was collected with an AC signal of 1.5 V at a scanning frequency of 1 Hz. Moreover, to evaluate the evolution of wake-up ferroelectricity in Ca:HfO$_2$, local switching spectroscopy (SS) PFM measurements were realized on a pristine point for 10 cycles with an AC signal of 2 V and DC sweep of ±8 V. Then, using the same location, a "PFM fatigue test" was carried out by applying first 2 cycles of DC poling at +10 V and −10 V for 5 seconds each, and repeating the local switching measurements.

3 Results and discussion

3.1 Thermal characteristics of the precursor solution and its components

In metallo-organic decomposition (MOD), the final quality of the deposited metal oxide is determined by the thermal behavior of the precursor solution and its components. Therefore, several elements of the fabrication of Ca:HfO$_2$ films were thermally analyzed under air-flow.

Because of its good stability in open conditions, hafnium 2,4-pentanedionate (Hf(acac)$_4$) is regularly employed in MOD chemistry to prepare HfO$_2$ films. In Fig. 2(a), the thermogravimetric (TA, blue), differential thermogravimetric (DTA, black), and differential scanning calorimetry (DSC, red) analyses are shown for as-received Hf(acac)$_4$. Initially, Hf(acac)$_4$ is stable, but suffers an endothermic, 35% mass loss starting at 130 °C
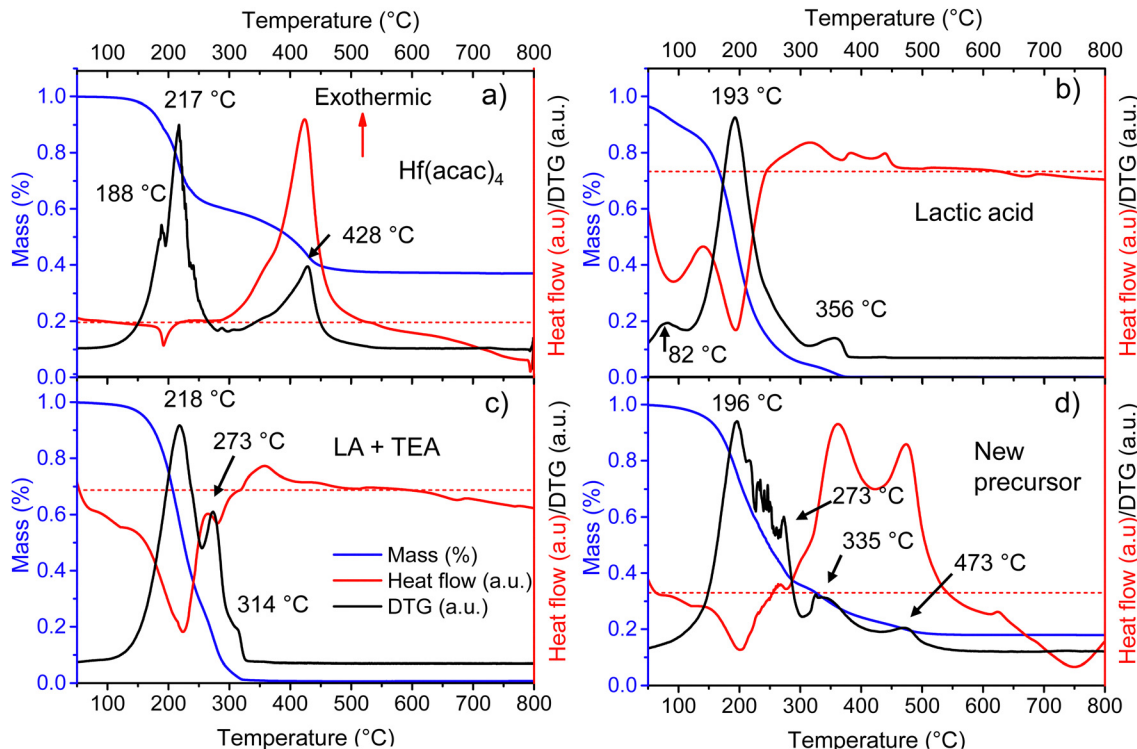

Fig. 2 TA(blue)/DTA(black)/DSC(red) curves for (a) as received 2,4-pentanedionate hafnium precursor, (b) as-received lactic acid (90%), (c) evaporated IPA + LA + TEA at 120 °C for 5 hours, and (d) Ca:HfO$_2$ evaporated precursor solution containing Hf(acac)$_4$, Ca(acac)$_2$, IPA, LA and TEA at 80 °C for a couple of hours. All measurements were carried out under an air flow of 100 ml min^{-1}. The red dotted line establishes the zero value for the heat flow measurement.

1122 | *J. Mater. Chem. C*, 2023, **11**, 1119–1133

This journal is © The Royal Society of Chemistry 2023

with maxima at 188 and 217 °C. A second, highly exothermic, significant mass loss is found at 428 °C. At a temperature of 800 °C, the mass of the residues accounts for 37.0% of the initial value. The theoretical yield for HfO_2 after the full oxidation of $Hf(acac)_4$ is 35.5% (considering a purity of 97%). Therefore, the observed residues might be composed of HfO_2, other impurity oxides and carbonized organic matter. Because of the high yield, the endothermic event at around 200 °C is an organic decomposition step without loss of hafnium metal. In the past, the study of the decomposition of metal acetylacetonates in an N_2 atmosphere has demonstrated the production of acetylacetone, acetone, CO_2 and even methane as byproducts.[25,39,40] On the contrary, it is expected that the highly exothermic event with maximum at 428 °C causes the complete oxidation of the initial compound and that most of the organic matter is finally released as CO_2 and H_2O.

It is known that Hf^{4+} and Zr^{4+} can be stabilized in aqueous media by some carboxylic acids, which act as mono-, bi- or multidentate ligands.[41,42] In a few solvents, apart from IPA, we observed that the dissolution of $Hf(acac)_4$ was only achieved after adding lactic acid and triethylamine. While the amount and type of solvent can be varied, the minimum molar ratios needed for the total solubilization of the Hf precursor were 1 : 4.3 : 8.4, corresponding to $Hf(acac)_4$/TEA/LA, respectively. This same ratio is also effective for the dissolution of the precursor of the doping metal element in small amounts $(Ca(acac)_2)$. The solution was put in reflux at 90–100 °C for 4 hours to ensure the total dissolution of any small salt nuclei. Reduced processing temperature ensures the stability of precursors.

To shed light on the thermal behavior of the new precursor solution, some of its components were analyzed independently. Three endothermic mass loss events were detected for as-received LA at 82, 193, and 356 °C (Fig. 2(b)). The events likely correspond to the evaporation of water and methanol, lactic acid, and lactide, respectively.[43] All initial mass is lost after 370 °C. The LA used for this study is a racemic mixture of L and D lactic acid with a purity of 90%, where the remaining components are mainly water, and traces of methanol and lactide. Thermal analysis was also tried for triethylamine, but this was not possible due to its high volatility even at room temperature.

To evaluate the interaction between the organic additives a metal-free precursor solution was obtained by mixing the corresponding amounts of IPA, LA, and TEA, without adding the metal 2,4-pentanedionates. The mixture was then evaporated for a few hours at 120 °C on a hot plate in an open atmosphere to remove IPA. Thermal analysis of the viscous residues is shown in Fig. 2(c). Two endothermic mass loss events can be found at 218 and 273 °C. A third, very small mass loss event can also be detected at 314 °C. It is known that amines (A) and carboxylic acids (C) can form complexes involving 2, 3, or 4 molecules through hydrogen bonding. Depending on the conditions, complexes of $A_1{:}C_2$ are usually more stable. The formation of the complexes increases significantly the boiling points of the mixtures and decreases their volatility.[31,44] For this

study, the TEA and LA mixture corresponds to a molar ratio of almost 1 : 2 ($A_1 : C_2$). In Fig. 2(c), the origin of the two peaks at 218 and 273 °C is most likely related to the separation and evaporation of a lactic acid + triethylamine complex. The mixture did not produce residues above 330 °C.

From a full, Hf and Ca-containing precursor solution, a small volume was separated and allowed to evaporate for a few hours at 120 °C on a hot plate in open conditions. The viscous, homogeneous, and slightly yellowish liquid residue was thermally characterized (Fig. 2(d)). Several endothermic, mass loss events, all related to evaporation, are found between 196 and 273 °C. The first mass loss, occurring at 196 °C is most likely related to the evaporation of LA, as was the case for pure lactic acid (Fig. 2(b)). The second evaporation, at 273 °C, might indicate the presence of an $A_1{:}C_2$ molecular complex as in Fig. 2(c). The other small mass loss events between 196 and 273 °C are probably related to the evaporation of released species from the total or partial replacement of acetylacetone groups surrounding the metal atoms. In Fig. 2(d), the following mass loss events at 335 and 473 °C are highly exothermic and none of them coincide with the exothermic decomposition temperature of pure $Hf(acac)_4$ at 428 °C (Fig. 2(a)). Thus, it might indicate that the LA + TEA modified Hf precursor suffers from decomposition in two distinct steps, with a temperature difference of 133 °C. Due to the instability of nitrogenated organic-hafnium compounds, the first decomposition step at 335 °C could be related to pyrolysis of N-containing species (like products of TEA breakup) and LA.[26,27] The second step at 473 °C might be due to total gasification to CO_2 and H_2O of carbonized oligomers produced by heating. No further mass loss is observed after 570 °C.

3.2 Phase stabilization by thermal processing

In Fig. 3, GIXRD diffractograms for different annealing temperatures at various holding times are shown. Moreover, the film thickness effect was also evaluated. For a $Ca{:}HfO_2$ film of 54 nm, a temperature of 700 °C for 90 s stabilized the cubic phase of HfO_2 (square symbols in Fig. 3(a)). The claim is based on the diffraction powder file shown in Fig. 3(h). However, although we will mostly refer to the cubic phase, it is difficult to establish if the tetragonal (Fig. 3(g)) or orthorhombic phases are present. This is because of the close resemblance of the three phases of HfO_2 (all with a fluorite structure) with just slight variations of the crystalline parameters, producing Bragg reflection at very close angles.[7] Therefore, most probably our $Ca{:}HfO_2$ films are composed of a mixture of phases, including an orthorhombic phase. At an annealing temperature of 800 °C held for 60 s (Fig. 3(b)), the 54 nm $Ca{:}HfO_2$ film crystallized into the cubic phase, but a small signal from the (111) plane at 31.7° of the monoclinic structure was also observed. A further increase of annealing time to 90 s at 800 °C made a few other m-phase reflections visible (Fig. 3(c)).

When the same rapid thermal annealing conditions are applied to thicker $Ca{:}HfO_2$ films of 90 nm (Fig. 3(d)–(f)), the crystallization of the monoclinic phase tends to be favored. As shown in Fig. 3(d), annealing at 700 °C for 90 s produces
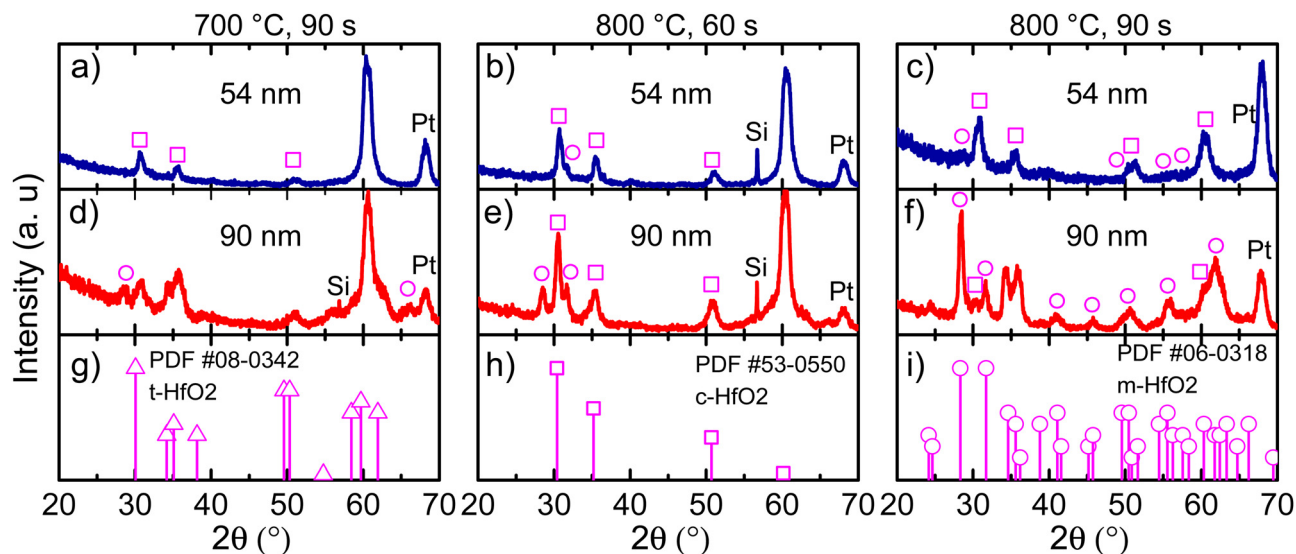
This journal is © The Royal Society of Chemistry 2023

J. Mater. Chem. C, 2023, 11, 1119–1133 | 1123

Fig. 3 GIXRD data for 54 nm Ca:HfO$_2$ films annealed at (a) 700 °C for 90 s, (b) 800 °C for 60 s, (c) 800 °C for 90 s, and for 90 nm Ca:HfO$_2$ films annealed at (d) 700 °C for 90 s, (e) 800 °C for 60 s, and (f) 800 °C for 90 s. Powder diffraction files for tetragonal (triangles), cubic (squares), and monoclinic (circles) phases are shown in (g), (h) and (i), respectively.

diffraction patterns of mixed m-phase with c- and/or t-phases. When the temperature is increased to 800 °C and held for 60 s, the presence of a predominantly c-phase with an m-phase as the secondary phase becomes evident (Fig. 3(e)). Finally, for a thick film annealed for 90 s at 800 °C, the m-phase becomes the predominant crystalline structure (Fig. 3(f)). This is consistent with the expectation that a smaller crystalline size can stabilize the fluorite structure with respect to the m-phase.[45] Therefore, it is expected that the increase in the annealing temperature or holding time and the augmentation of film thickness have affected the phase transformation in favor of a stable monoclinic structure.[46] We have indeed observed this same trend in our work. An estimation of the crystallite size for films of predominantly c-phase produced values of around 8 nm (Scherrer's equation). Usually, the HfO$_2$ crystallization into the ferroelectric orthorhombic phase has been ascribed to a transformation from t- to o-structure either during deposition or electric-field cycling.[47] Even so, for HfO$_2$ films obtained by CSD, transformation from c- to o-phase has also been reported.[14] It is even possible to partially transform the m-phase to the o-phase under low-oxygen stoichiometric conditions and applied bias, which reduces the energy for transformation to the polar o-phase.[10,48]

Interestingly, the intensity of the (−111) Bragg reflection at 28.5° of the m-phase appears in different proportion to a powdered material (Fig. 3(i)). Growth in a preferential direction likely causes the effect. Moreover, for both 54 and 90 nm thick films, an intense diffraction plane appears at 60.3° upon annealing conditions of 700 °C for 90 s and 800 °C for 60 s. This angular position corresponds well to the (311) diffraction plane of the c-phase of HfO$_2$, but its intensity is unusual and can also imply a preferential growth direction. No reflections of any other possible structures (given the multi-layer stacking Ca:HfO$_2$/Pt/Ti/SiO$_2$/Si of the films) such as Si, Pt, Ti, TiO$_2$, SiO$_2$ of CaO are expected to occur at this position. Similar observations have been made in a few other

reports of HfO$_2$ prepared by chemical solution deposition. In the work of Schenk *et al.*,[49] the crystallization of La:HfO$_2$ with preferred orientation was ascribed to heterogeneous nucleation of the cubic phase within the thickness of each deposited layer. This creates a multi-layer superstructure with density gradients, which helps to stabilize the higher symmetry phases of HfO$_2$. Also, in the work of Starschich, although it was not explicitly mentioned, relatively intense peaks of the cubic phase at 50° (220) and 60° (311) were observed for Y:HfO$_2$.[15] From X-ray reflectivity measurements, the density of one of our Ca:HfO$_2$ films annealed at 800 °C for 90 s was estimated to be 8.34 g cm^{-3}. For La:HfO$_2$ films fabricated by CSD, Schenk calculated a density of 8.0 g cm^{-3}, which is only 80% of the expected value (9.6 g cm^{-3}). Given the nature of CSD processes, the lower density is ascribed to porosity in the films caused by voids left during decomposition of organic residues during annealing.[4]

3.3 Quality of interfaces

For thin films applied in microelectronics, surface and interface morphology control is essential. Although typically Atomic Force Microscopy (AFM) is only useful for surface imaging, it can also provide a glimpse of the dynamics during HfO$_2$ crystallization. As stated in Section 2.3, RTA was applied asymmetrically. The back side of the platinized silicon substrates were put in direct contact with TiO$_2$-coated graphite plates, while the top surfaces were exposed to infrared and visible radiation through a quartz window. The goal of this arrangement was to maximize the heating of the HfO$_2$ films while avoiding any possible change in the morphology of the bottom Pt electrode. The result of this treatment on the surface morphology can be observed in Fig. 4. For Ca:HfO$_2$ films of 54 nm in thickness, the increasingly harsh annealing conditions produced the growth and fusion of grains on the surface. Initially, clear grain boundaries can be observed for the film
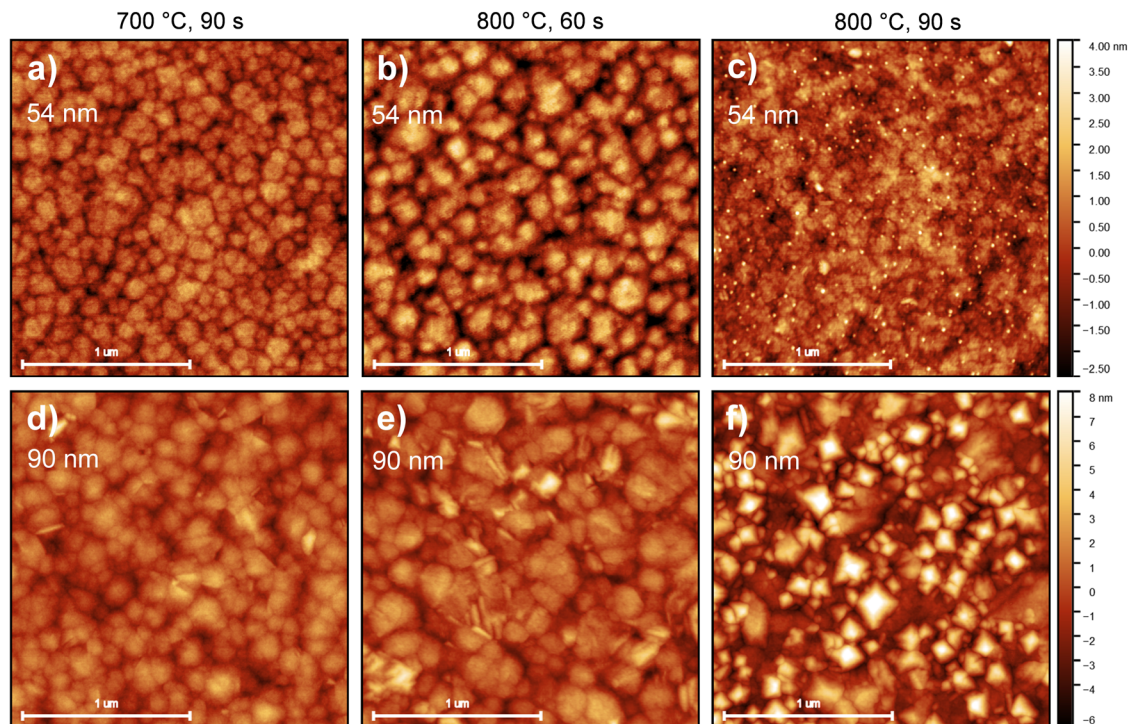
1124 | *J. Mater. Chem. C*, 2023, **11**, 1119–1133

This journal is © The Royal Society of Chemistry 2023

Fig. 4 AFM images for surfaces of 54 nm Ca:HfO$_2$ films annealed at (a) 700 °C for 90 s, (b) 800 °C for 60 s, (c) 800 °C for 90 s, and for 90 nm Ca:HfO$_2$ films annealed at (d) 700 °C for 90 s, (e) 800 °C for 60 s, and (f) 800 °C for 90 s.

annealed at 700 °C for 90 s (Fig. 4(a)). An increase in annealing temperature up to 800 °C for 60 s causes growth of the grains through coalescence (Fig. 4(b)). When the holding time is increased to 90 s at 800 °C, the grains are fused, and grain boundaries are less evident (Fig. 4(c)). In addition, very small, rounded particles appear to nucleate on the surface, coinciding with the appearance of the monoclinic phase in GIXRD (Fig. 3(c)). The Root Mean Square (RMS) roughness slightly increases from 0.67 to 0.69 and then to 0.78 nm, respectively. A similar trend is found for 90 nm thick Ca:HfO$_2$ films. Nevertheless, for the thicker films, even from the beginning, the grains seem to be larger, and elongated crystals appear on the surface. For the film annealed at 800 °C for 90 s (Fig. 4(f)) the crystals are not elongated, but rather pyramids with a well-defined orientation. Again, GIXRD data showed the emergence of the monoclinic phase for these annealing conditions. In addition, the surface becomes heavily fused. The roughness of these thicker films increases from 1.2 nm to 1.5 nm, and 2.4 nm, respectively. Furthermore, to have an estimation of grain size behavior, the AFM images were analyzed by the watershed method with the open software Gwyddion.[50] Values of 10.7, 12.1 and 14.9 nm were obtained for 54 nm films, and 10.9, 13.8 and 17.0 nm for 90 nm ones, which corresponds to 60 s at 700 °C, 60 s at 800 °C and 90 s at 800 °C for both cases. The trend in grain size clearly shows an increase with annealing conditions. Also, the grain growth rate is faster for the thicker films, which means that as the thickness of Ca:HfO$_2$ films is increased, the control of grain size is restricted to narrower conditions.

Considering the observations made in GIXRD (Fig. 3), the observed nucleation of crystals on the surface, the increase in roughness, and the raise in grain size seem to be related to the nucleation and growth of the m-phase of HfO$_2$. This result is due to the cell volume difference between the m-phase and the higher symmetry phases.[20,51] Moreover, the pyramidal crystals pointing out of plane can be a confirmation of the preferential orientation of the crystallites, with the (−111) direction out of plane, as suggested by GIXRD analysis. In the next section we investigate how these differences affect the ferroelectric properties of the different Ca:HfO$_2$ films.

3.4 Ferroelectric wake-up conditioning

Wake-up conditioning has been carried out to evaluate the ferroelectric characteristics of the films. As stated in Section 2.4, rectangular pulses of 2.78 MV cm^{-1} were applied at 1 kHz for 10^3–10^4 times. Top platinum electrodes of 100 μm in diameter were probed. Polarization and current density curves *versus* electric field are shown in Fig. 5 for Ca:HfO$_2$ films with 54 nm thickness. After wake-up, films annealed at 700 °C for 90 s (Fig. 5(a) and (d)) show the behavior of a dielectric with linear polarization and a rectangular *J*–*E* behavior.[52,53] However, upon closer evaluation, a small, pinched hysteresis loop can be found after wake-up at 10^4 cycles. The slight ferroelectric behavior of the film is evidenced better after endurance tests at 10^5 cycles (Fig. S2 in the ESI†). This observation means that an annealing temperature of 700 °C is enough to cause the nucleation of the stable ferroelectric o-phase. Similar observations have been made for other doped-HfO$_2$ systems.[20,51,54] Nonetheless, the
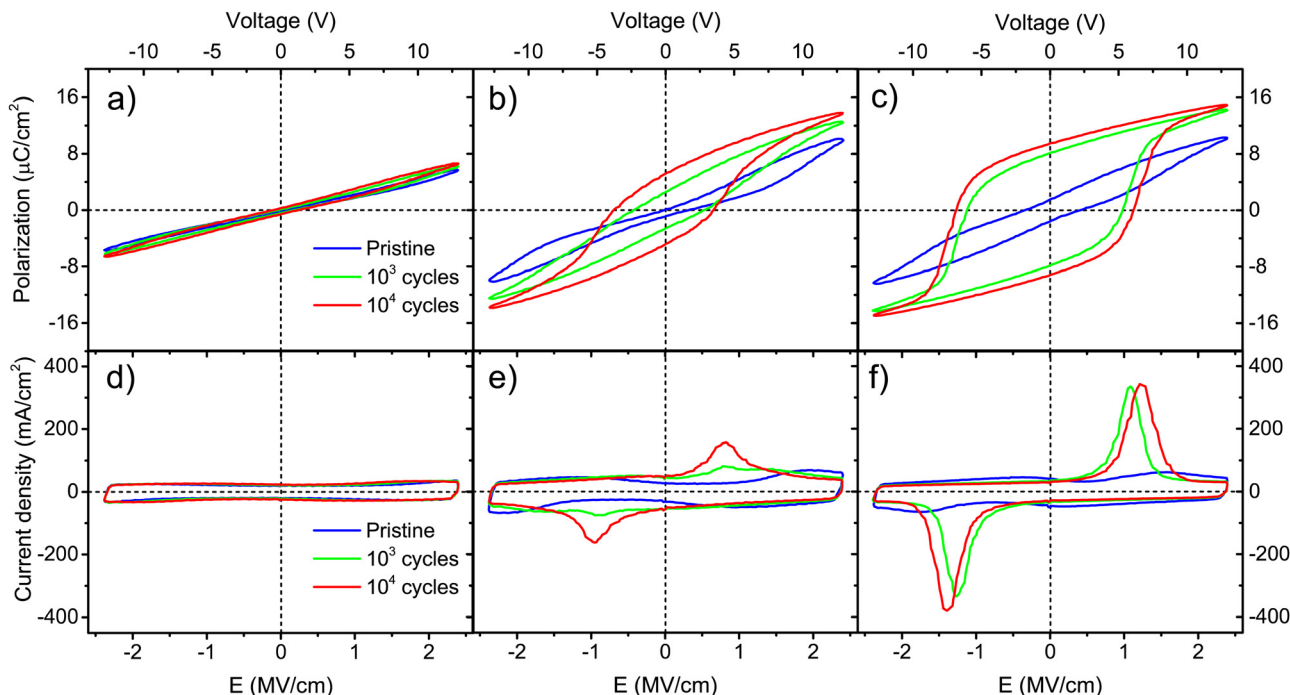
Fig. 5 Polarization and current density *vs.* electric field strength for 54 nm Ca:HfO$_2$ films annealed at: (a) and (d) 700 °C for 90 s, (b) and (e) 800 °C for 60 s, and (c) and (f) 800 °C for 90 s. The films received wake-up conditioning at 1 kHz for 0 (pristine), 10^3, and 10^4 cycles at 2.78 MV cm^{-1}.

ferroelectric wake-up effect becomes more evident for films annealed at 800 °C for 60 s (Fig. 5(b) and (e)). Polarization and current density loops start to be formed after 10^3 cycles, but a definite ferroelectric behavior, with switching currents peaks, is observed at 10^4 cycles. At this point, it is worth mentioning that a hysteretic polarization loop is not enough for some materials to prove ferroelectricity. Leakage and parasite currents can cause the appearance of an open loop, which can be interpreted as ferroelectric polarization.[55] Likewise, high P_r values can be artificially obtained from leaky capacitors, thus this is not enough to prove ferroelectricity. Therefore, in *J–E* plots it is important to look for both spontaneous polarization of a ferro-electric material and low leakage of the dielectric. In some cases, high remnant polarization values are being taken as the only indication of the strength of a ferroelectric material. However, P_r values are calculated from integration of transient currents, and artificially high P_r values can easily be obtained from leaky capacitors.[52,53,56] At least in the literature regarding doped-HfO$_2$ films obtained by chemical solution methods, P_r values are seemingly often overestimated. We include a brief discussion of this in Section 3 of the ESI.† For Ca:HfO$_2$ films annealed at 800 °C for 90 s (Fig. 5(c) and (d)) and cycled for 10^3 and 10^4 times,

the ferroelectricity is robust after 10^3 wake-up cycles. The *J–E* graph shows strong switching peaks at +1.2 MV cm^{-1} and −1.4 MV cm^{-1}. Moreover, due to the relatively large thickness of all the films, the current density *versus* filed characteristics remain rectangular, as expected for a capacitor, without indication of leakage. To the best of our knowledge, apart from the present work, Starschich is the only one who has shown well-saturated polarization loops for doped-HfO$_2$ synthesized by CSD.[14,15]

In Table 1, different ferroelectric indicators are shown for the Ca:HfO$_2$ films that exhibited a wake-up effect. For films of 54 nm annealed at 800 °C, an increase in holding time from 60 to 90 s caused the coercive field (E_{c+}) to shift to higher values, from 0.8 to 1.2 MV cm^{-1}. This was also the case for the remnant polarization (P_{r+}), which increased from 5.2 to 9.5 μC cm^{-2}, respectively.

For thicker Ca:HfO$_2$ films of 90 nm, a purely dielectric behavior was found for the films annealed at 700 and 800 °C for 90 s and cycled for 10^3 and 10^4 times at 2.78 MV cm^{-1} (Fig. 6(a), (d), (c) and (f), respectively). However, the sample annealed at 800 °C for 60 s showed a clear ferroelectric behavior with a well-saturated polarization loop and strong switching peaks (Fig. 6(b) and (c)). For this thicker film, the shorter

Table 1 Properties of Ca:HfO$_2$ devices that showed ferroelectric wake-up after 10^4 cycles of 2.78 MV cm^{-1} rectangular pulses at 1 kHz

Annealing temperature (°C)	Time (s)	Thickness (nm)	Current peak max (+) (μA cm^{-2})	Current peak max (−) (μA cm^{-2})	E_{c+} (MV cm^{-1})	E_{c-} (MV cm^{-1})	P_{r+} (μC cm^{-2})	P_{r-} (μC cm^{-2})
800	60	54	157	163	0.8	1.0	5.2	4.8
800	90	54	343	381	1.2	1.4	9.5	9.2
800	60	90	523	559	1.1	1.4	11.1	10.5

1126 | *J. Mater. Chem. C*, 2023, **11**, 1119–1133

This journal is © The Royal Society of Chemistry 2023

annealing time restricted the growth of the grain size. In Table 1, it is seen that the E_{c+} of this film was 1.1 MV cm^{-1} and it attained a slightly higher P_{r+} value of 11.1 µC cm^{-2} compared to the thinner saturated film (9.5 µC cm^{-2}, annealed for 90 s). The study of these thicker samples can help to highlight the following points: (i) although CSD methods have been more successful in producing thick, ferroelectric, and piezoelectric HfO$_2$ films, a layer-by-layer annealing process has often had to be adopted.[49] Our current CSD method could benefit from such an approach but, for the moment, we consider that good results can be obtained with fewer processing steps. (ii) The annealing step is one of the most important steps towards achieving control of ferroelectric HfO$_2$. Wang *et al.* found that minor changes in RTA processing conditions extensively affect the ferroelectricity of the films.[54] A gradual increase in ferroelectricity with increasing both annealing temperature and holding time was found for our Ca:HfO$_2$ films of 54 nm. This is, the film annealed at 700 °C for 90 s did not show significant ferroelectric behavior, but the film annealed at 800 °C for 60 s achieved a P_{r+} of 5.2 µC cm^{-2} and the film heat-treated at 800 °C for 90 s attained a P_{r+} of 9.5 µC cm^{-2}. For thicker films (90 nm), ferroelectricity appeared in narrower annealing conditions. In addition, the annealing time needed to achieve ferroelectricity was 30 s shorter for the thicker Ca:HfO$_2$ film than for the thinner one. These effects are due to the propensity of HfO$_2$ to crystallize into the monoclinic phase when its vertical direction growth is not restricted, which favors the growth of the crystallites.[49] This is important for piezoelectric applications, where the control of ferroelectricity in thick HfO$_2$ films is a key point.[4]

The ferroelectricity of the Ca:HfO$_2$ films can be related to the results obtained by GIXRD (Fig. 3) and AFM analysis (Fig. 4). It has been commonly reported that, under certain conditions, the o-phase can be stabilized just before it transforms into the m-phase.[54] All 54 nm Ca:HfO$_2$ films crystallized into the c- or t-phase. However, a small increase in m-phase was also observed for higher annealing temperatures and holding times. The m-phase is non-polar and has a lower dielectric constant compared to higher symmetry phases, thus its appearance is regularly avoided. For thicker Ca:HfO$_2$ films, evidence of the m-phase was observed at all annealing conditions, but it became predominant at 800 °C for 90 s. The m-phase presence in AFM images was evidenced by the appearance of pyramid-shaped crystals on the surface of Ca:HfO$_2$ films (Fig. 4(f)). During electrical field cycling, amorphous and crystalline HfO$_2$ is subjected to stress and strain. Due to the presence of dopants stabilizing high symmetry phases, the intermediate ferroelectric orthorhombic phase can be achieved.[19] According to Lederer *et al.*, initially amorphous or semicrystalline Hf-based films react differently to the applied field. Semicrystalline films show better ferroelectric properties after wake-up than fully crystallized ones.[57] Our Ca:HfO$_2$ films show the behavior of a semicrystalline film. For the ferroelectric film of 90 nm, despite the presence of a small fraction of m-phase, a good, saturated response was achieved. Thus, it seems possible that a higher, tailored P_r value could be obtained at slightly shorter holding times at 800 °C.

To the best of our knowledge, only one other report deals with ferroelectric HfO$_2$ stabilized with calcium doping.[20] In their work, Yao *et al.* stabilized the higher symmetry phases of HfO$_2$ by varying Ca concentrations through a different precursor
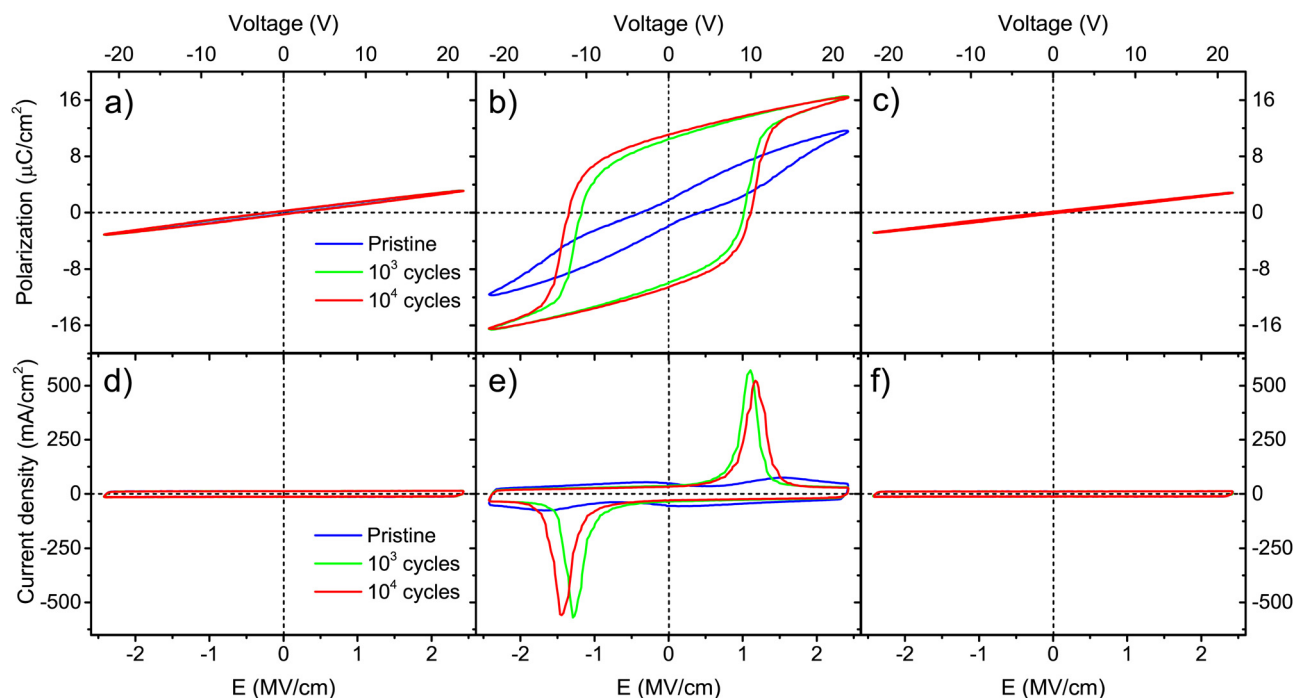

Fig. 6 Polarization and current *vs.* electric field strength for 90 nm Ca:HfO$_2$ films annealed at (a) and (d) 700 °C for 90 s, (b) and (e) 800 °C for 60 s, and (c) and (f) 800 °C for 90 s. The films received wake-up conditioning at 1 kHz for 0 (pristine), 10^3, and 10^4 cycles at 2.78 MV cm^{-1}.

solution and annealing conditions. They report a maximum P_r value of 10.5 μC cm^{-2} for a 35 nm Ca:HfO$_2$ film doped with 4.8 mol% Ca and cycled 10^4 times at 100 Hz. They clearly evidence the wake-up of ferroelectricity in Ca:HfO$_2$. However, the smaller thickness of those films is likely responsible for the lack of saturation of the polarization loops and the larger coercive fields (2 MV cm^{-1}, instead of our maximum 1.4 MV cm^{-1}).

According to theoretical and experimental studies, the polar o-phase of HfO$_2$ can only be stabilized by the presence of oxygen vacancies.[58,59] This decreases the energy difference between the more stable m-phase and the higher symmetry phases. When the effect of oxygen vacancies in phase stabilization of HfO$_2$ is studied, the polar o-phase sits in between the m- and t-phase, where m- has the lowest oxygen vacancies concentration.[10] Coherently with the latter, it has been reported that the redistribution of defects, particularly oxygen vacancies, by application of wake-up cycling, can help to stabilize the ferroelectric orthorhombic structure through field-induced phase transformation.[60] Often, the oxygen vacancies (which in this material are known to be positively charged) are generated near the electrode interfaces, or migrate there upon the application of the electric field. The defects at any location can create pinning of domains, but most commonly they induce a built-in bias field that suppresses the polarization of ferroelectric dipoles. During field cycling, a redistribution or recombination (oxygen vacancies and oxygen interstitials for example) of defects occurs, lowering the built-in field and allowing for the polarization of dipoles to the same direction. This is why pinched hysteresis loops can appear for pristine samples,

but upon defect diffusion and recombination they open up to form more typical ferroelectric loops.[20,48,51]

3.5 Ferroelectricity in thinner Ca:HfO$_2$ layers

One advantage of HfO$_2$-based ferroelectrics is that, contrary to other ferroelectrics, it can sustain a remnant polarization even at small thicknesses. Also, HfO$_2$ exhibits larger coercive fields compared to other ferroelectrics, which means that higher voltages are required to disrupt its polarization. Moreover, hafnia tends to produce a stronger ferroelectric behavior with a decrease in thickness. Indeed, the highest remnant polarization values in the literature have been obtained for films of a few nanometers. Thin films with strong ferroelectricity are of particular interest for high-density FeRAM devices, which are usually obtained by physical deposition methods like PLD and ALD. Nonetheless, such methods are also more complicated than CSD.

We evaluated our chemical processing for the deposition of ferroelectric thin films of HfO$_2$. Following the same procedures, we deposited a thin 18 nm Ca:HfO$_2$ layer on platinized silicon and annealed it at 800 °C for 90 s (roughness of 0.56 nm). The top electrodes were also deposited and measured but they were in short circuit. More likely, this issue arises from some contamination during deposition under room conditions. Therefore, we investigated the local ferroelectric properties using instead PFM, which utilizes the electrically conductive tip of an AFM (radius of 10–30 nm) in contact mode as the top electrode. As discussed in the previous section, HfO$_2$ based ferroelectrics often require AC and/or DC conditioning to show ferroelectric behavior. To induce wake-up of the films using
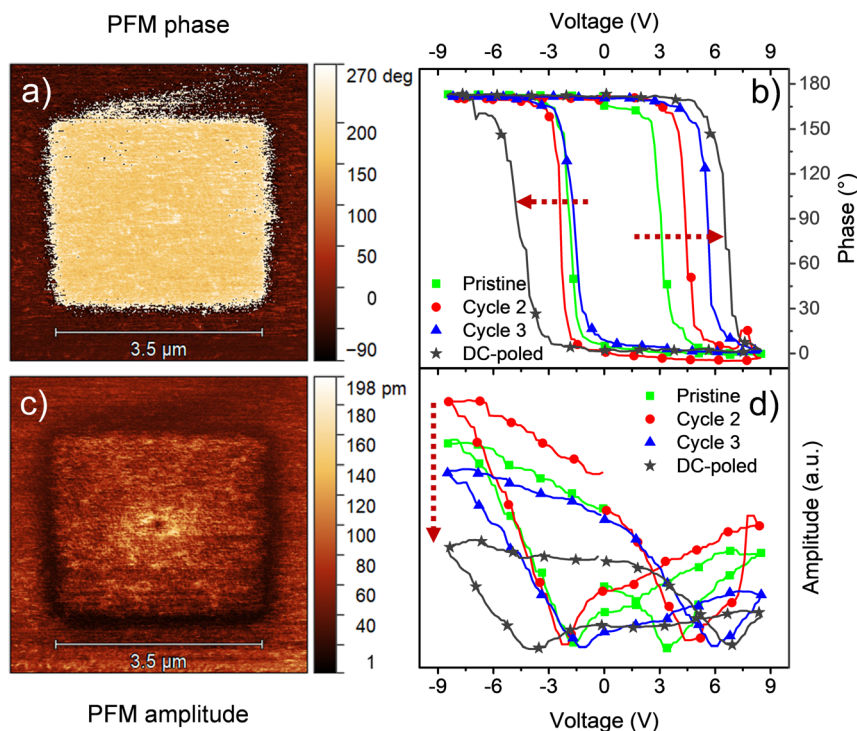

Fig. 7 PFM (a) phase and (c) amplitude imaging, and local PFM measurements for (b) phase and (d) amplitude for an 18 nm Ca:HfO$_2$ film annealed at 800 °C for 90 s.

1128 | *J. Mater. Chem. C*, 2023, **11**, 1119–1133

This journal is © The Royal Society of Chemistry 2023

PFM equipment, a DC +10 V bias has been applied to the tip while scanning a squared region of 3.5 μm × 3.5 μm at a frequency of 0.5 Hz. Later, a larger area of 5 μm × 5 μm was PFM-scanned with an AC signal of 1.5 V. As presented in Fig. 7, both phase and amplitude images were obtained. Clearly, the phase signal shows the switching of ferroelectric domains with applied DC poling to the 3.5 μm × 3.5 μm area. The brighter color represents polarization out of plane (up), indicating that the original polarization was pointing down. Moreover, the amplitude image measures the piezoelectric response of the films. The areas with polarization pointing up and down are expected to have the same piezoelectric response, while no piezoelectric response is expected at the domain wall.[23] This is indeed consistent with the observations.

Local switching spectroscopy (SS) measurements were made on a point on the pristine area. During the very first local SS measurement (green lines in Fig. 7(b) and (d)), the phase exhibits a narrow loop with 180° phase difference and the amplitude presents a butterfly loop, as expected for a piezoelectric Ca:HfO$_2$ film. However, the butterfly loop is highly asymmetric, and it does not close after the first cycle. For a second cycle (red line), the phase loop moves to larger coercive voltages and the piezoelectric signal increases but the ends do not meet (first and last measurement points in the loop). These measurements, thus, also show that ferroelectric response of Ca:HfO$_2$ increases with electrical processing, in agreement with the wake-up effect discussed in Section 3.4. For the third SS cycle (blue line), the ends of the amplitude loop meet, but the signal is also reduced. Moreover, the asymmetry is deepened for the positive bias and the coercive voltage also rises. In contrast, a SS loop obtained after DC poling at ±10 V displays a significant increase in the coercive voltage with respect to the non-poled area, but its amplitude diminishes in intensity and becomes very asymmetric (gray line). Thus, the material under the PFM tip can be considered fatigued. The observed asymmetry in the loops is likely related to the difference in work function between the bottom Pt electrode of the sample and the Co/Cr coating of the PFM scanning tip. Nevertheless, other effects such as a built-in field, or interfacial effects as charge accumulation during the SS measurement cannot be disregarded.[61]

3.6 Fatigue measurements

One of the major challenges for the development of ferroelectric HfO$_2$ is to increase its endurance. Following the same protocol of rectangular pulses for the ferroelectric wake-up of our Ca:HfO$_2$ films, we have performed fatigue measurements at different frequencies for up to 10^7 cycles with electric fields of 2.78 MV cm^{-1}. As stated in Section 2.4, all Ca:HfO$_2$ micro-capacitors were initially woken-up at a frequency of 1 kHz with application of 10^3 bipolar cycles. In Fig. 8, endurance results are shown. For both, 54 nm and 90 nm films, we found that pristine Ca:HfO$_2$ capacitors are barely ferroelectric with a small P_r value. However, they soon become ferroelectric after the application of field cycling at 1 kHz 10^3 times. Upon further cycling at 1 kHz, the P_r value slightly increases. Nonetheless, the P_r peaks at 10^4 cycles and then the polarization starts to decrease. Remarkably, ferroelectric fatigue (decrease in switching currents) sets in faster
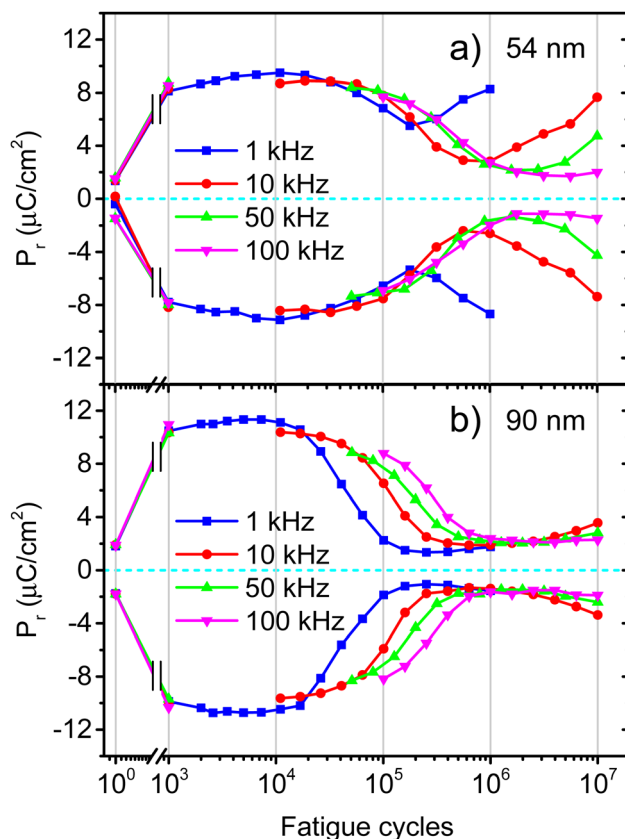

Fig. 8　Fatigue measurements at varying frequencies for Ca:HfO$_2$ films of (a) 54 nm annealed at 800 °C for 90 s, and (b) 90 nm annealed at 800 °C for 60 s. All measured capacitors were woken-up at a frequency of 1 kHz.

for the thicker Ca:HfO$_2$ film (Fig. 8(b)), but the thinner film becomes dielectrically fatigued (increase in leakage) already at around 10^5 cycles. These effects are more evident when looking at Fig. 9. After 10^5 cycles, the 54 nm Ca:HfO$_2$ film shows a decrease in P_r due to reduced switching currents. Also, the maximum of the switching currents are displaced to larger E_c values, which can be related to the creation of new defects (mainly oxygen vacancies) that, if sufficiently high, create conductive filaments where current flows more freely.[62] In addition, if there is a transformation from the o- to the m-phase, this would create regions of lower dielectric permittivity, thus affecting the distribution of the electric field. Therefore, creation of non-polar dead-layers within the film or at the electrodes, and pinning of domains by defect generation can increase E_c while lowering the P_r.[48] At 10^6 cycles, there is no evidence of switching currents. Instead, the exponential current at high field strength is evidence of dielectric fatigue through a surge in leakage. Although the leakage might look comparatively small, it produces an extrinsic P_r value of 8 μC cm^{-2}, which is an artifact and does not arise from ferroelectric switching (green lines in Fig. 9(a) and (c)). Besides, a "banana" loop appears in the corresponding polarization figure, which is evidence of a leaky dielectric.[55] A similar trend is observed for the thicker Ca:HfO$_2$ film of 90 nm (Fig. 9(b) and (d)). Nonetheless, the ferroelectric fatigue is severe even at 10^5 cycles, for which switching currents
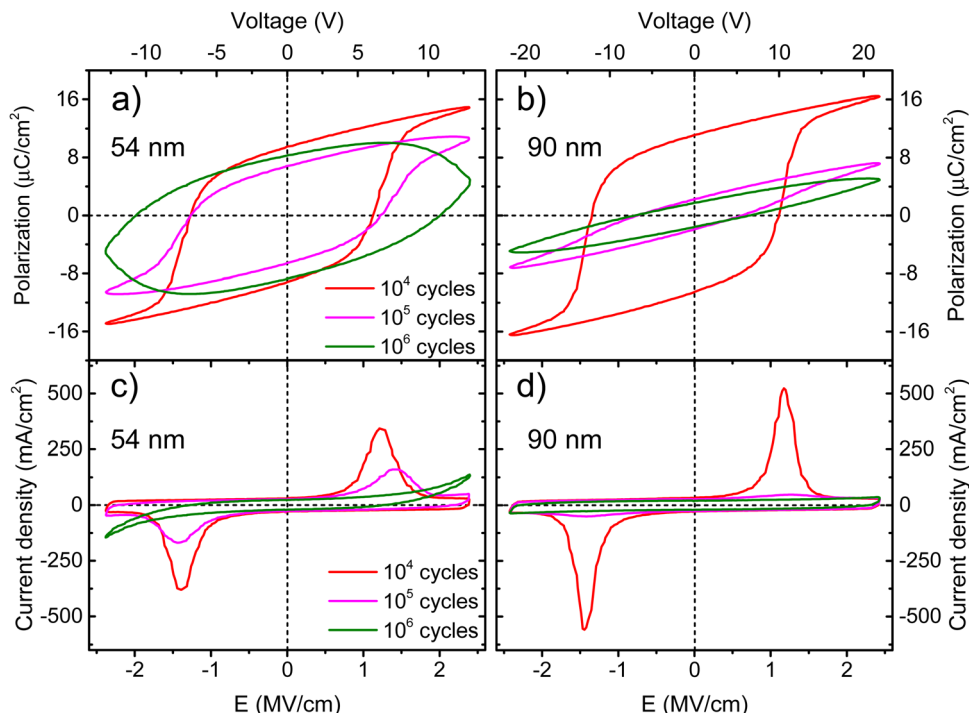
Fig. 9 Polarization and current density *vs.* electric field strength for 54 nm Ca:HfO$_2$ films ((a) and (c)) annealed at 800 °C for 90 s, and 90 nm Ca:HfO$_2$ films ((b) and (d)) annealed at 800 °C for 60 s. The films were fatigued at 1 kHz for an increasing number of cycles at 2.78 MV cm^{-1}.

are barely noticeable. Further cycling produces the markers of a slightly leaky dielectric, which also causes the polarization loop to look slightly open. The higher resilience of the thicker Ca:HfO$_2$ against leakage is expected due to better shielding of weak/hot spots. In this case, it is easy to distinguish ferroelectric from dielectric fatigue, a distinction that gets increasingly complicated for leaky ferroelectrics, often leading to overestimation of the P_r values (see the discussion in Section 3 of the ESI†). Although in the work of Yao *et al.* only 35 nm Ca:HfO$_2$ films were tested at a frequency of 10 kHz, and we found a similar endurance behavior for our thin Ca:HfO$_2$ films.[20]

It is well known in ferroelectric HfO$_2$ literature that endurance depends on the applied frequency, the electric field's strength, and the shape of the pulses.[62] Fatigue tests at higher frequencies cause less ferroelectric wear down for the same number of cycles because the material is exposed to high electric fields for shorter periods. Despite this, our Ca:HfO$_2$ films show ferroelectric fatigue at less than 10^6 cycles for all tested frequencies (Fig. 8). Furthermore, fatigue has been associated with increased leakage, generating new charge defects and pinning of the domain walls.[48] The latter holds for our thinner Ca:HfO$_2$ film. However, the thicker film fatigues ferroelectrically faster than the thinner one, as a transformation from the o- to m-phase can take place during field cycling.[63] Therefore, if possible, a way to delay the o- to m-phase transition should be found for increasing the endurance of doped-HfO$_2$.

3.7 Implications of the new chemical route for ferroelectric hafnia synthesis

In most reports involving the fabrication of ferroelectric films of HfO$_2$ or ZrO$_2$ by chemical solution deposition, the metal acetylacetonates are dissolved in propionic acid or its mixture with propionic anhydride (the last requiring well-controlled ambient conditions, typically in an N$_2$ glovebox). For such reports, it has not been explained how the dissolution of the original Zr or Hf acetylacetonates takes place, but it is most probably due to the formation of metal propionates and of acetates derived from decomposition of the acetylacetonates at high reflux temperatures.[29] The carboxy groups in the carboxylates are coordinated to the metal center.[64] The decomposition of such modified precursors proceeds through different mechanisms than those of the pure metal acetylacetonates.[29] Depending on the modified precursor, the synthesis of the metal oxides can result in advantages or disadvantages for the final device fabrication and performance.[15,65]

It is known from ALD and chemical vapor deposition (CVD) precursor studies that nitrogen in nitrogenated organic compounds can coordinate directly to the hafnium atom to form volatile substances. Nevertheless, these precursors are unstable and highly prone to hydrolysis,[26,27] making them difficult to handle. Instead, some researchers have shown that heteroleptic precursors (consisting of more than one type of ligand bound to the metal atom) can have higher stability than homoleptic ones.[26] Therefore, given the thermal behavior of our modified Hf precursor, we might be dealing with a heteroleptic precursor in liquid form. However, this needs further analysis. A deeper understanding could also result in the increase of substances that are capable of dissolving hafnium precursors in less harsh and restricted conditions.

Our results show that the new chemical route offers less toxicity, higher flexibility, and more adaptability, being useful

1130 | *J. Mater. Chem. C*, 2023, **11**, 1119–1133

This journal is © The Royal Society of Chemistry 2023

for larger scale deposition techniques, where control of the rheology of solution is mandatory.[66] Although triethylamine is toxic compared to the other components of the new precursor solution, it is used in minimal amounts (3.4% by volume). This low content limits the toxicity of the solution as a whole. Besides, less toxic amines or substitutes could be researched to replace triethylamine.[41] Furthermore, the new solution possesses higher flexibility because the dissolution of the precursor salt is achieved by additives and not by the solvent. Thus, different solvents can be used. The latter also provides a new chemical route with better adaptability. Viscosity, reactivity, and rheology can be tuned by using different amounts and types of solvents; thus, different fabrication techniques can be applied. Moreover, other additives can be used in the new solution. We have tried this for glycerol, citric acid, nitric acid, and mono-ethanolamine, which did not affect the solubility of the precursor. Furthermore, it is also essential to use an easy-to-handle, non-toxic, and simple solutions to avoid corrosion, clogging, or damage of the equipment components. The synthesis of ferro-electric hafnia films by ultrasonic spray-coating is in progress.

Finally, future and extensive research can be carried out on the proposed precursor solution by studying different parameters such as drying temperatures,[15] heating ramps,[54] diverse dopants, layer-by-layer annealing,[67] thickness constraint,[49] wake-up free synthesis,[54,67] *etc.* Therefore, there is plenty of promising research to improve this low-toxicity chemical solution route for ferro-electric HfO_2 synthesis.

4 Conclusions

A new precursor chemical solution for the fabrication of ferroelectric doped-HfO_2 films, particularly Ca:HfO_2, has been introduced in this work. Compared to other routes reported in the literature, our solution has low toxicity. Lactic acid and triethylamine were used as solubilizing additives in small amounts in an isopropanol solvent. However, isopropanol can be interchanged with other alcohols. It was demonstrated upon thermal analysis that the modified precursor does not follow the same decomposition path as the starting metal compound. Therefore, our solution follows a different decomposition route. Moreover, different additives can be used to tailor the properties of the solution and make it suitable for the fabrica-tion of HfO_2 films by other, larger scale deposition techniques like spray coating and ink-jet printing. We found that high, saturated ferroelectricity with no indication of high leakage can be induced in Ca:HfO_2 (5 at%) by rapid thermal annealing under an $Ar:O_2$ atmosphere (1:1). The temperature and time of annealing are critical in determining the ferroelectric response of HfO_2 films. While thin films of 54 nm show an increasingly higher ferroelectric response with increasing tem-perature and time, thick films (90 nm) exhibit ferroelectric behavior only under a narrow window at a shorter time (30 s less than the thinner film at 800 °C). From GIXRD and AFM measurements, this difference seems to arise from the nuclea-tion and growth of the non-polar monoclinic phase within the

orthorhombic phase. In thick films, the monoclinic phase can grow more unrestrictedly. This also affects the difference in ferroelectric endurance between thin and thick Ca:HfO_2 films. Although the initial P_r and dielectric endurance of 90 nm Ca:HfO_2 films at different frequencies were high (9.5 and 11.1 $\mu C\ cm^{-2}$), they also suffered from loss of the ferroelectric response much faster. Despite the loss of switching currents at above 10^5 fatigue cycles, it is remarkable that 90 nm Ca:HfO_2 films prepared by our accessible chemical method exhibited strong and well saturated ferroelectricity. Our proposed chemical solution route could be effectively used for studies with other dopants and processing conditions. Moreover, it can also be used for fabrication of ZrO_2 based films.

Author contributions

Conflicts of interest

There are no conflicts of interest to declare.

Acknowledgements

References

1 T. S. Böscke, J. Müller, D. Bräuhaus, U. Schröder and U. Böttger, *Appl. Phys. Lett.*, 2011, **99**, 102903.

This journal is © The Royal Society of Chemistry 2023

J. Mater. Chem. C, 2023, **11**, 1119–1133 | 1131

2 S. Starschich and U. Böttger, *J. Appl. Phys.*, 2018, **123**, 044101.

3 T. Francois, C. Pellissier, S. Slesazeck, V. Havel, C. Richter, A. Makosiej, B. Giraud, E. T. Breyer, M. Materano, P. Chiquet, M. Bocquet, L. Grenouillet, E. Nowak, U. Schroeder, F. Gaillard, J. Coignus, P. Blaise, C. Carabasse, N. Vaxelaire, T. Magis, F. Aussenac and V. Loup, *Demonstration of BEOL-compatible ferroelectric Hf0.5Zr0.5O2 scaled FeRAM co-integrated with 130nm CMOS for embedded NVM applications*, IEEE, San Francisco, 2019.

4 T. Schenk, N. Godard, A. Mahjoub, S. Girod, A. Matavz, V. Bobnar, E. Defay and S. Glinsek, *Phys. Status Solidi RRL*, 2020, **14**, 1900626.

5 S. Kim, J. Y. Park, S. Go, H. S. Kwon, W. Y. Choi and S. Kim, *Solid State Electron.*, 2021, **175**, 107956.

6 S. Kirbach, K. Kuhnel and W. Weinreich, *Piezoelectric Hafnium Oxide Thin Films for Energy-Harvesting Applications*, IEEE, Cork, 2018, vol. 2018-July.

7 H. Chen, X. Zhou, L. Tang, Y. Chen, H. Luo, X. Yuan, C. R. Bowen and D. Zhang, *Appl. Phys. Rev.*, 2022, **9**, 011307.

8 O. Ohtaka, H. Fukui, K. Funakoshi, W. Utsumi, T. Irifune and T. Kikegawa, *High Press. Res.*, 2002, **22**, 221–226.

9 Y. Wei, P. Nukala, M. Salverda, S. Matzen, H. J. Zhao, J. Momand, A. S. Everhardt, G. Agnus, G. R. Blake, P. Lecoeur, B. J. Kooi, J. Íñiguez, B. Dkhil and B. Noheda, *Nat. Mater.*, 2018, **17**, 1095–1100.

10 K. Z. Rushchanskii, S. Blügel and M. Ležaić, *Phys. Rev. Lett.*, 2021, **127**, 087602.

11 S. Mueller, J. Mueller, A. Singh, S. Riedel, J. Sundqvist, U. Schroeder and T. Mikolajick, *Adv. Funct. Mater.*, 2012, **22**, 2412–2417.

12 U. Schroeder, E. Yurchuk, J. Müller, D. Martin, T. Schenk, P. Polakowski, C. Adelmann, M. I. Popovici, S. V. Kalinin and T. Mikolajick, *Jpn. J. Appl. Phys.*, 2014, **53**, 08LE02.

13 *Ferroelectricity in Doped Hafnium Oxide: Materials, Properties and Devices*, ed. U. Schröder, C. Seong Hwang and H. Funakubo, Woodhead Publishing, Duxford, 1st edn, 2019.

14 S. Starschich and U. Boettger, *J. Mater. Chem. C*, 2017, **5**, 333–338.

15 S. Starschich, D. Griesche, T. Schneller and U. Böttger, *ECS J. Solid State Sci. Technol.*, 2015, **4**, P419–P423.

16 T. Shiraishi, K. Katayama, T. Yokouchi, T. Shimizu, T. Oikawa, O. Sakata, H. Uchida, Y. Imai, T. Kiguchi, T. J. Konno and H. Funakubo, *Appl. Phys. Lett.*, 2016, **108**, 262904.

17 M. Hyuk Park, H. Joon Kim, Y. Jin Kim, T. Moon and C. Seong Hwang, *Appl. Phys. Lett.*, 2014, **104**, 072901.

18 R. Batra, T. D. Huan, G. A. Rossetti and R. Ramprasad, *Chem. Mater.*, 2017, **29**, 9102–9109.

19 H. Yang, K. Park, H. J. Lee, J. Jo, H. Park, N. Park, J. Park and J. H. Lee, *Inorg. Chem.*, 2020, **59**, 5993–5999.

20 Y. Yao, D. Zhou, S. Li, J. Wang, N. Sun, F. Liu and X. Zhao, *J. Appl. Phys.*, 2019, **126**, 154103.

21 U. Schroeder, C. Richter, M. H. Park, T. Schenk, M. Pešić, M. Hoffmann, F. P. G. G. Fengler, D. Pohl, B. Rellinghaus, C. Zhou, C.-C. Chung, J. L. Jones and T. Mikolajick, *Inorg. Chem.*, 2018, **57**, 2752–2765.

22 T. Mimura, T. Shimizu and H. Funakubo, *Appl. Phys. Lett.*, 2019, **115**, 032901.

23 S. Kim and J. Hong, *Ceram. Int.*, 2017, **43**, S158–S161.

24 S. Nakayama, H. Funakubo and H. Uchida, *Jpn. J. Appl. Phys.*, 2018, **57**, 4–9.

25 G. V. Bazuev and L. D. Kurbatova, *Russ. Chem. Rev.*, 1993, **62**, 981–989.

26 T. Blanquart, J. Niinistö, M. Ritala and M. Leskelä, *Chem. Vap. Deposition*, 2014, **20**, 189–208.

27 M. G. Walawalkar, A. Kottantharayil and V. R. Rao, *Synth. React. Inorg., Met.-Org., Nano-Met. Chem.*, 2009, **39**, 331–340.

28 *Handbook of Reactive Chemical Hazards*, ed. P. G. Urben and M. J. Pitt, Elsevier, Amsterdam, 8th edn, 2017.

29 S. Petit, S. Morlens, Z. Yu, D. Luneau, G. Pilet, J. L. Soubeyroux and P. Odier, *Solid State Sci.*, 2011, **13**, 665–670.

30 S. Zheng, Z. Zhao, Z. Liu, B. Zeng, L. Yin, Q. Peng, M. Liao and Y. Zhou, *Appl. Phys. Lett.*, 2020, **117**, 0–6.

31 A. Kumar, A. Thakur and P. S. Panesar, *Rev. Environ. Sci. Bio/Technol.*, 2019, **18**, 823–853.

32 C. J. Diliegros Godines, C. G. Torres Castanedo, R. Castanedo Pérez, G. Torres Delgado and O. Zelaya Ángel, *Sol. Energy Mater. Sol. Cells*, 2014, **128**, 150–155.

33 M. A. Badillo-Ávila, R. Castanedo-Pérez, G. Torres-Delgado, J. Márquez-Marín and O. Zelaya-Ángel, *Mater. Sci. Semicond. Process.*, 2018, **74**, 203–209.

34 P. Tundo, P. Anastas, D. S. Black, J. Breen, T. J. Collins, S. Memoli, J. Miyamoto, M. Polyakoff and W. Tumas, *Pure Appl. Chem.*, 2000, **72**, 1207–1228.

35 J. Fu and Y. Wu, *Chem. – Eur. J.*, 2021, **27**, 9967–9987.

36 V. D. Moreno-Regino, C. G. Torres-Castanedo, J. S. Arias-Cerón, M. A. Badillo-Ávila, J. Márquez-Marín, R. Castanedo-Pérez, O. Zelaya-Ángel and G. Torres-Delgado, *J. Alloys Compd.*, 2019, **803**, 1168–1177.

37 B. Franco-Linton, R. Castanedo-Pérez, G. Torres-Delgado, J. Márquez-Marín and O. Zelaya-Ángel, *Mater. Sci. Semicond. Process.*, 2016, **56**, 302–306.

38 G. Martinez-Saucedo, R. Castanedo-Perez, G. Torres-Delgado, A. Mendoza-Galvan and O. Z. Angel, *Mater. Sci. Semicond. Process.*, 2017, **68**, 133–139.

39 J. Von Hoene, R. G. Charles and W. M. Hickam, *J. Phys. Chem.*, 1958, **62**, 1098–1101.

40 H. M. Ismail, *Powder Technol.*, 1995, **85**, 253–259.

41 T. Qiang, J. Zhao and J. Li, *Microporous Mesoporous Mater.*, 2018, **257**, 162–174.

42 A. Tonosaki and T. Nishide, *Appl. Phys. Express*, 2010, **3**, 125801.

43 A. Komesu, P. F. Martins Martinez, B. H. Lunelli, J. Oliveira, M. R. Wolf Maciel and R. Maciel Filho, *J. Chem.*, 2017, **2017**, 1–7.

44 N. S. Nhlapo, W. W. Focke and E. Vuorinen, *Thermochim. Acta*, 2012, **546**, 113–119.

45 G. Sharma, S. V. Ushakov and A. Navrotsky, *J. Am. Ceram. Soc.*, 2018, **101**, 31–35.

46 H. Liang, J. Xu, D. Zhou and S. Ren, *J. Alloys Compd.*, 2021, **861**, 158241.

1132 | *J. Mater. Chem. C*, 2023, **11**, 1119–1133

This journal is © The Royal Society of Chemistry 2023

47 P. Jiang, Q. Luo, X. Xu, T. Gong, P. Yuan, Y. Wang, Z. Gao, W. Wei, L. Tai and H. Lv, *Adv. Electron. Mater.*, 2021, **7**, 2000728.

48 M. Pešić, F. P. G. Fengler, L. Larcher, A. Padovani, T. Schenk, E. D. Grimley, X. Sang, J. M. LeBeau, S. Slesazeck, U. Schroeder and T. Mikolajick, *Adv. Funct. Mater.*, 2016, **26**, 4601–4612.

49 T. Schenk, A. Bencan, G. Drazic, O. Condurache, N. Valle, B. El Adib, N. Aruchamy, T. Granzow, E. Defay and S. Glinsek, *Appl. Phys. Lett.*, 2021, **118**, 1–16.

50 P. Klapetek, D. Nečas and C. Anderson, Gwyddion user guide, https://gwyddion.net.

51 Z. Li, D. Zhou, J. Wang, N. Sun and W. Zhang, *J. Appl. Phys.*, 2022, **131**, 074101.

52 L. Jin, F. Li and S. Zhang, *J. Am. Ceram. Soc.*, 2014, **97**, 1–27.

53 T. Schenk, E. Yurchuk, S. Mueller, U. Schroeder, S. Starschich, U. Böttger and T. Mikolajick, *Appl. Phys. Rev.*, 2014, **1**, 0–14.

54 J. Wang, D. Zhou, W. Dong, Y. Yao, N. Sun, F. Ali, X. Hou and F. Liu, *Adv. Electron. Mater.*, 2021, **7**, 2000585.

55 J. F. Scott, *J. Phys.: Condens. Matter*, 2008, **20**, 021001.

56 T. Schenk, U. Schroeder and T. Mikolajick, *IEEE Trans. Ultrason. Eng.*, 2015, **62**, 596–599.

57 M. Lederer, S. Abdulazhanov, R. Olivo, D. Lehninger, T. Kämpfe, K. Seidel and L. M. Eng, *Sci. Rep.*, 2021, **11**, 1–7.

58 Y. Zhou, Y. K. Zhang, Q. Yang, J. Jiang, P. Fan, M. Liao and Y. C. Zhou, *Comput. Mater. Sci.*, 2019, **167**, 143–150.

59 M. Hoffmann, U. Schroeder, T. Schenk, T. Shimizu, H. Funakubo, O. Sakata, D. Pohl, M. Drescher, C. Adelmann, R. Materlik, A. Kersch and T. Mikolajick, *J. Appl. Phys.*, 2015, **118**, 072006.

60 S. Starschich, S. Menzel and U. Böttger, *Appl. Phys. Lett.*, 2016, **108**, 032903.

61 L. Collins and U. Celano, *ACS Appl. Mater. Interfaces*, 2020, **12**, 41659–41665.

62 S. Starschich, S. Menzel and U. Böttger, *J. Appl. Phys.*, 2017, **121**, 154102.

63 S. S. Fields, S. W. Smith, P. J. Ryan, S. T. Jaszewski, I. A. Brummel, A. Salanova, G. Esteves, S. L. Wolfley, M. D. Henry, P. S. Davids and J. F. Ihlefeld, *ACS Appl. Mater. Interfaces*, 2020, **12**, 26577–26585.

64 Z. Czech and M. Wojciechowicz, *Eur. Polym. J.*, 2006, **42**, 2153–2160.

65 S. Starschich, D. Griesche, T. Schneller, R. Waser and U. Böttger, *Appl. Phys. Lett.*, 2014, **104**, 202903.

66 N. Godard, M. A. Mahjoub, S. Girod, T. Schenk, S. Glinšek and E. Defay, *J. Mater. Chem. C*, 2020, **8**, 3740–3747.

67 S. Samanta, G. Anoop, H. Joh, W. Seol, S. M. Park, S. Unithrattil, J. Y. Lee, T. Y. Kim, H. Kim, J. Yeom, S. Hong and J. Y. Jo, *Adv. Mater. Interfaces*, 2021, **8**, 2100907.

This journal is © The Royal Society of Chemistry 2023

J. Mater. Chem. C, 2023, **11**, 1119–1133 | **1133**